Nanoscale

PAPER

View Article Online
View Journal | View Issue

Check for updates

Cite this: *Nanoscale*, 2022, **14**, 15679

Solution processed, vertically stacked heterostructured diodes based on liquid-exfoliated WS_2 nanosheets: from electrode-limited to bulk-limited behavior†

Shixin Liu, Er-Xiong Ding, Adam G. Kelly, Luke Doolan, Cian Gabbett, Harneet Kaur, Jose Munuera, Tian Carey, James Garcia and Jonathan N. Coleman *

Vertically stacked metal–semiconductor-metal heterostructures, based on liquid-processed nanomaterials, hold great potential for various printed electronic applications. Here we describe the fabrication of such devices by spray-coating semiconducting tungsten disulfide (WS_2) nanosheets onto indium tin oxide (ITO) bottom electrodes, followed by spraying single-walled carbon nanotubes (SWNTs) as the top electrode. Depending on the formulation of the SWNTs ink, we could fabricate either Ohmic or Schottky contacts at the WS_2/SWNTs interface. Using isopropanol-dispersed SWNTs led to Ohmic contacts and bulk-limited devices, characterized by out-of-plane conductivities of $\sim 10^{-4}$ S m^{-1}. However, when aqueous SWNTs inks were used, rectification was observed, due to the formation of a doping-induced Schottky barrier at the WS_2/SWNTs interface. For thin WS_2 layers, such devices were characterized by a barrier height of ~0.56 eV. However, increasing the WS_2 film thickness led to increased series resistance, leading to a change-over from electrode-limited to bulk-limited behavior at a transition thickness of ~2.6 μm. This work demonstrates that Ohmic/Schottky behavior is tunable and lays the foundation for fabricating large-area 2D nanosheet-based solution-deposited devices and stacks.

Received 29th July 2022,
Accepted 14th October 2022

DOI: 10.1039/d2nr04196k

rsc.li/nanoscale

Introduction

Two-dimensional (2D) materials have been extensively studied over the past two decades due to their diversity and range of interesting properties.[1,2] For example, focusing on electronic properties, silver nanosheets and MXenes are metallic,[3,4] graphene is a semimetal,[5] transition metal dichalcogenides such as tungsten disulfide (WS_2), are semiconducting[6] while boron nitride (BN) is an insulator.[7] This electronic diversity is very exciting as it means that different 2D materials can be used as different parts of electronic devices.

In particular, over the last few years, much work has focused on using 2D nanosheets as elements in printed electronic devices with the ultimate aim of achieving mobilities competitive with the best organic devices. In addition, there is considerable interest in all-printed, all-nanomaterial,[8] devices where different device parts, *e.g.* active material, electrodes and dielectric, could be printed from different 2D materials or combinations of 2D and non-2D materials.[9]

Producing printed or solution-deposited devices requires inks which consist of 2D nanosheets (or other nanomaterials) dispersed in liquids. Liquid phase exfoliation (LPE) is a method which employs ultra-sonication of various bulk layered materials in liquids to produce dispersions of 2D nanosheets in large quantities.[10,11] Such nanosheet dispersions can be used as inks and processed into thin films which, at the nanoscale, consist of disordered networks of nanosheets.[3,7,8,12] To date, many printing and solution-deposition methods have been used in this way, including ink-jet printing,[13,14] spin-coating,[15] electrophoretic deposition,[16] spray coating.[7] In particular, spray coating is a method which is relatively versatile and is able to efficiently fabricate large-area networks on various types of substrates.[17] Solution-processing of nanosheet networks enables the low-cost and facile fabrication of printed electronic devices. Solution-deposited networks of semiconducting nanosheets have demonstrated their potential in applications such as transistors,[8] photodetectors[18] and chemical sensors.[19]

The above-mentioned devices are usually fabricated in a planar manner and consist of relatively large area networks of

---

School of Physics, CRANN & AMBER Research Centres, Trinity College Dublin, Dublin 2, Ireland. E-mail: colemaj@tcd.ie; Tel: +353 (0) 1 8963859

† Electronic supplementary information (ESI) available. See DOI: https://doi.org/10.1039/d2nr04196k

semiconducting nanosheets with laterally positioned electrodes. Conduction is usually in the plane of the network and the channel length (defined as the distance between electrodes) is typically tens to hundreds of micrometers. The in-plane (IP) conductivity ranges from 10^{-1} to 10^{-9} S m^{-1} and is generally limited by the inter-nanosheet junction resistance.[12] Because of the long channel length and low film thickness, such networks tend to display a high channel resistance much larger than the metal/semiconductor contact resistance. This is an important point as it means that such networks are always bulk-limited, *i.e.* the current flowing is limited by the resistance of the network rather than any contact effects such as Schottky barriers.[20] This makes it virtually impossible to obtain electrical rectification in planar networks as such effects arise from metal–semiconductor contacts.

One way to obtain contact limited effects, such as Schottky barriers, in printed or solution-deposited nanosheet networks is to fabricate vertical heterostructures consisting of stacked metal–semiconductor-metal (MSM) layers (A.K.A. a sandwich structure) where the semiconductor is a nanosheet network. The channel length in this case corresponds to the thickness of the semiconductor network, which in principle could be reduced to as low as a few nanometers. This means the resistance of the semiconductor layer can be much smaller than that in a planar device. By reducing this channel resistance below the contact resistance, it should be possible to produce contact-limited devices once appropriate metals are used.

However, problems are still associated with fabricating such thin, stacked devices. First, short-free nanosheet networks are mandatory for this kind of device structure. Although increasing network thickness could minimize pinholes associated with network non-uniformity, production of thin short-free networks is still a challenge.[12] Another difficulty lies in the porous nature of solution-deposited networks[8] which can allow penetration of metal atoms during top-electrode deposition, resulting in shorting even for uniform, continuous films. In addition, for solution-deposited top electrodes, nanosheet re-dispersion during deposition can lead to poor metal–semiconductor interfaces and shorting in thin films.[12] This makes it difficult to prepare stacked devices and means relatively few of these have been reported in the literature. To date, a small number of vertically-stacked printed or solution-deposited devices, including capacitors,[7,21,22] memristors,[23,24] and photodetectors,[3,25,26] have been reported which combine LPE nanosheets and solution-processed top electrodes. Avoiding shorts is usually achieved by using thick semiconducting layers,[12] often with negative impacts on performance.

Up to now, most vertically stacked devices with either solution-processed or evaporated top electrodes show Ohmic behavior. This is due to the high series resistance associated with the thick semiconducting nanosheet networks, leading to bulk-limited behavior regardless of the size of the Schottky barrier. However, while non-Ohmic behaviors have been observed in printed $Ag/MoS_2/MoO_x/Ag$[23] devices, to our knowledge only Farbod *et al.*[27] have realized Schottky diodes in a simple MSM (FTO/phosphorene/Al) stack. Thus, Schottky diodes from LPE nanosheet networks alone are still very poorly investigated. It remains an important question whether Schottky devices can be reliably fabricated and if their electrical behaviors might be manipulated, by varying the contacting metal or semiconductor thickness.

In this study, we demonstrate a reliable method to fabricate vertically-stacked MSM devices by sequentially spraying networks of semiconducting WS_2 nanosheets and carbon nanotubes. These devices are short-free down to a WS_2 network thickness of 500 nm. In addition, their properties can be tuned from electrode- to bulk-limited both by modifying the nanotube ink and by varying the thickness of the WS_2 network.

Results

Material characterizations

All devices were prepared by sequential spraying of nanomaterial inks prepared in-house. The WS_2 nanosheet dispersion was prepared by LPE in the solvent isopropanol (IPA). Using IPA allows the formation of a reasonably stable dispersion with a relatively high yield of nanosheets and, because of its low boiling point, facilitates further device fabrication without solvent exchange. As is typical for LPE, immediately after exfoliation the dispersion contained poly-disperse nanosheets with a wide distribution of lateral size and thickness.[28] Thus, a two-step liquid cascade centrifugation (LCC) procedure was used to narrow the distribution.[29,30] Since large and thick nanosheets tend to be rigid,[12] and so may lead to a nanosheet network with high porosity and large pores, they were discarded by centrifuging the dispersion after exfoliation at 2 krpm for 2 h. Meanwhile, to avoid few-layered WS_2 with thickness-varying bandgaps,[31,32] small and thin nanosheets were also discarded by a 6 krpm centrifugation. The transmission electron microscopy (TEM) image of exfoliated nanosheets obtained after LCC is shown in Fig. 1A. Many nanosheets were seen, all similar in size, confirming our successful exfoliation and size-selection.

Two types of SWNT dispersion were obtained by probe sonicating P3-SWNTs (Carbon solutions) in IPA and sodium dodecyl benzene sulfonate aqueous solution ($SDBS/H_2O$), respectively. Briefly, 0.5 mg mL^{-1} SWNTs in 40 mL of water containing 5 mg mL^{-1} SDBS surfactant was probe-sonicated for 30 min to yield an aqueous dispersion. The dispersion was centrifuged at 6 krpm for 2 h to remove large aggregates and the supernatant collected (subsequently referred to as S-SWNTs dispersion). The IPA-suspended dispersion (I-SWNTs) was obtained by directly sonicating SWNTs powder in IPA with a concentration of 0.05 mg mL^{-1} for 4 h (no centrifugation was used). A low concentration and longer sonication time ensure that the dispersion can be stable at least for a few hours, which is required for spray coating. Fig. 1B and C show the morphology of SWNTs in IPA and $SDBS/H_2O$, respectively. Narrow and straight bundles were found in TEM images, indicating the SWNTs were well-dispersed in both

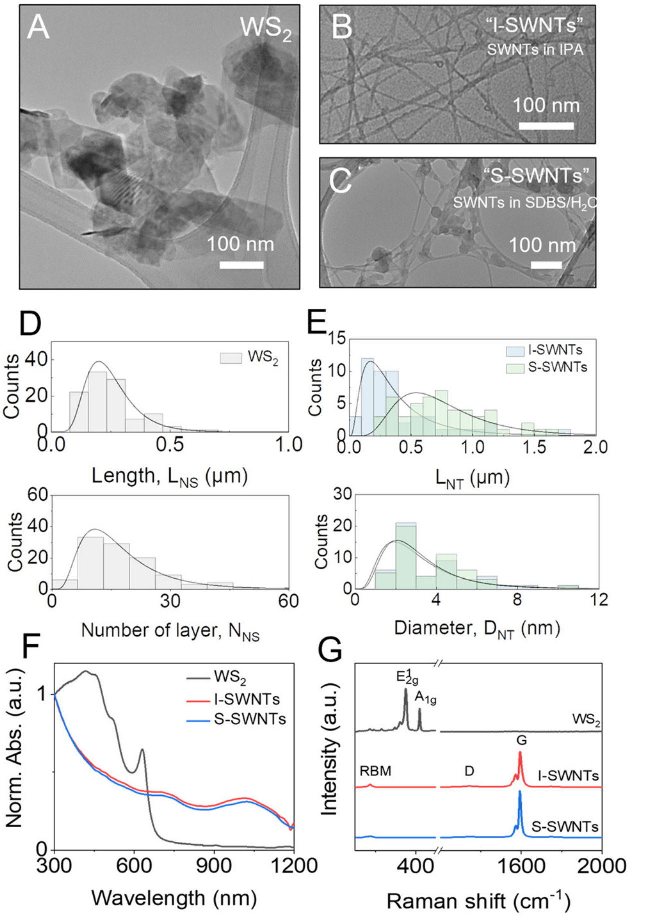

Fig. 1 Basic characterizations of WS$_2$ nanosheets and SWNTs. TEM images of WS$_2$ nanosheets (A), I-SWNTs (B) and S-SWNTs (C). (D) Statistical analysis of the lateral length L_{NS} and the number of layer N_{NS} of WS$_2$ nanosheets extracted from AFM images. (E) Statistical analysis of the length L_{NT} and diameter D_{NT} of SWNTs extracted from AFM images. Normalized UV-Vis-NIR absorption spectra (F) and Raman spectra (G) of WS$_2$, I-SWNTs and S-SWNTs.

media. The I-SWNTs present clean surfaces while polymeric residuals were visible on the surface of S-SWNTs possibly due to SDBS, which is notoriously difficult to remove.[33]

To determine the size and thickness distribution of nanosheets, the WS$_2$ and SWNTs dispersions were drop-casted on Si/SiO$_2$ substrates and characterized by atomic force microscopy (AFM). Their typical AFM images are shown in Fig. S1† insets. For WS$_2$, the statistical results were obtained by counting the size and thickness of more than 100 individual nanosheets and are shown in Fig. 1D. Most of the nanosheets are shorter than 500 nm with a mean length $\langle L_{NS}\rangle$ of 250 nm, which is in good agreement with the TEM images. The number of layers, N_{NS}, was obtained by dividing the nanosheet thickness by the apparent monolayer thickness (1.9 nm).[34] The mean layer number is $\langle N_{NS}\rangle = 17.5$. The nanosheet length is plotted against its thickness in Fig. S1A.† The aspect ratio (AR) defined as the length divided by the thickness was obtained from the histogram plot of nanosheet length divided by thickness L_{NS}/t_{NS}, shown in Fig. S1A.† The average AR is ~10. We note that these AR values are small compared to values of 20–40 reported previously for aqueous TMD dispersions,[28] probably due to the use of IPA in this study. The AFM result indicates the obtained WS$_2$ nanosheets are mostly multi-layered with a relatively medium size compared to its bulk counterpart, consistent with our requirements as mentioned above. The SWNTs were also characterized with AFM and the statistical results are shown in Fig. 1E. The mean length $\langle L_{NT}\rangle$ of S-SWNT is 771 nm, while that for I-SWNTs is 405 nm. The shorter nanotubes are caused by long time sonication in IPA. The mean diameter of nanotube bundles $\langle D_{NT}\rangle$ is around 3.2 nm for both I-SWNTs and S-SWNTs. The mean aspect ratios $\langle L_{NT}/D_{NT}\rangle$ for S-SWNTs and I-SWNTs are ~166 and ~322 (Fig. S1B and C†), respectively, which are both much larger than that of WS$_2$.

UV-Vis-NIR spectra of WS$_2$, I-SWNTs and S-SWNTs were collected, and the normalized absorption spectra are shown in Fig. 1F. Full spectra are presented in Fig. S2.† The characteristic A-exciton peak for WS$_2$ can be found at 637 nm. This peak position was known to be affected by the layer number of nanosheets due to confinement effects.[30] The mean nanosheet length $\langle L_{NS}\rangle$ and the number of layers $\langle N_{NS}\rangle$ can be derived from its extinction spectrum and are 283 nm and 20.5 (ESI, S2†), respectively, which are consistent with AFM statistical results.

The absorption peaks for I-SWNTs and S-SWNTs can be observed at around 700 nm and 1022 nm, corresponding to M_{11} metallic and S_{22} semiconducting characteristic peaks[35] respectively, with no obvious dependence on dispersing medium.

The WS$_2$ and SWNTs dispersions were drop-cast onto an Si/SiO$_2$ substrate to form films for Raman analysis as shown in Fig. 1G. The WS$_2$ characteristic modes at 349.5 and 418.5 cm^{-1} are found and correspond to its in-plane $E^1{}_{2g}$ and out-of-plane A_{1g} modes. For both SWNTs, characteristic peaks such as the radial breathing mode (RBM) at 170 cm^{-1}, disorder D band at 1345 cm^{-1}, and graphite (G) band at 1593 cm^{-1} can be seen.[36] There is very little difference in G band position for I-SWNTs and S-SWNTs, implying minimal doping by SDBS relative to IPA.

Device fabrication and morphological characterizations

Although we initially characterize in-plane devices, the main focus of this work is on devices in stacked geometries where current flow is out-of-plane. To this end, we use sequential spraying processes to fabricate vertically stacked, sandwich structure-type devices. These devices consist of a patterned ITO bottom electrode, then a network of semiconducting WS$_2$ nanosheets, followed by a top electrode. As we justify below, we use a network of carbon nanotubes as the top electrode, followed in some cases by a network of silver nanowires as a current collector. A schematic of the device structure is shown in Fig. 2A. ITO-coated glass was used as the substrate with the subsequent layers built up sequentially by layer-by-layer spray coating.

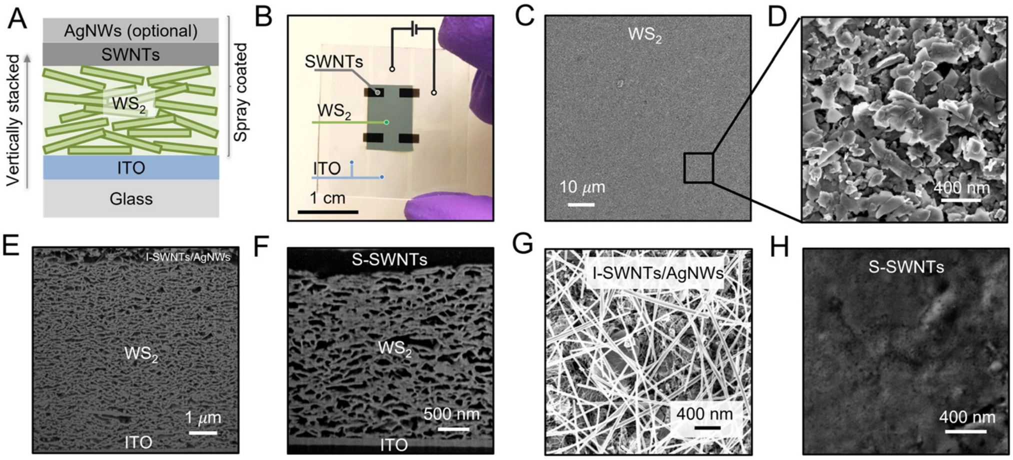

Fig. 2 (A) Schematic diagram of the device structure and fabrication. (B) Photograph of ITO/WS_2/S-SWNTs devices. Top-view SEM images of the spray coated WS_2 film (C), the WS_2 film with higher magnification (D). Cross-sectional SEM images of ITO/~6.5 μm WS_2/I-SWNTs (E) and ITO/~2.5 μm WS_2/S-SWNTs (F). Top-view SEM images of the double-layered I-SWNTs/AgNWs top electrode (G) and S-SWNTs electrode (H) on WS_2 film.

A common problem during sequential liquid-based depositions is the redispersion of the previously deposited layer during the deposition of the next layer before the deposited solvent has dried. This effect probably limits the minimum thickness of the semiconducting layer (*i.e.* the channel length) that can be achieved without shorts appearing between ITO and SWNT layers, as well as device reproducibility. We believe the likelihood of the formation of vertical shorts is highest when the top electrode is deposited by evaporation or sputtering. Metal atoms can diffuse through the porous interior of the network, perhaps at locally thin regions, leading to the formation of metallic filaments which can short the device. To avoid electrical shorts as well as achieving low semiconducting layer thickness, we propose this problem may be mitigated by using networks of high-aspect ratio conducting nanomaterials, such as nanotubes or nanowires, as the top electrode. Such extended structures could sit on top of the semiconducting nanosheet network without penetrating the pores of the network, bridging any locally thin regions and so avoiding the formation of vertical shorts.

To prove the feasibility of this approach, ITO-coated glass substrates were etched using diluted hydrochloride acid to create one long 2.5 cm × 0.6 cm ITO strip in the middle of the glass and four ITO patches on each corner of the slide (Fig. 2B). The distance between the strip and each patch is 1–2 mm. After solvent cleaning of the ITO-coated substrates, a WS_2 dispersion was sprayed on top of the ITO strip such that the ITO edge is covered by WS_2 film to avoid contact between ITO and the top electrode that will be sprayed later. The hotplate was set at 100 °C to enable fast evaporation of IPA. The obtained WS_2 film on ITO were then annealed at 200 °C in an argon-filled glovebox for 30 minutes to remove residual IPA and to improve the network's mechanical robustness. A range of WS_2 networks were deposited with thicknesses in the range of 500 nm to 9000 nm. For SWNT top electrode fabrication, the spray rate and the volume of SWNTs dispersion were carefully adjusted, and the hotplate temperature was also increased to facilitate solvent evaporation (experimental details are presented in ESI S1†). A shadow mask was used to pattern the top electrode and to allow each SWNTs electrode to partially cover the ITO/WS_2 and one of the individual ITO patches. Thus, electrical measurements of each ITO/WS_2/SWNTs device can be made through the main ITO strip and one patch. Four SWNT top electrodes were deposited per substrate. The device area is defined as the overlapping area between the ITO electrode, WS_2 and the SWNTs electrode, which is typically 2–4 mm^2. Using the above method, we have found that devices can be reproducibly fabricated. In the case of I-SWNTs top electrodes, AgNW networks were also deposited on top of the SWNTs to reduce the lateral resistance of the top electrode, as will be detailed in the following sections. A photograph of the obtained devices is shown in Fig. 2B.

Scanning electron microscopy (SEM) and an optical transmission scanner were used to investigate the morphology of the sprayed nanosheet networks. SEM images of WS_2 nanosheet networks are shown in Fig. 2C and D. The low-magnification image shows that nanosheets are uniformly deposited over a large area and form networks that appear to be pinhole-free. The zoomed-in SEM image in Fig. 2D shows that nanosheets are randomly stacked together, forming a porous, disordered network. The morphology of a thin WS_2 nanosheet network on glass slides was further investigated by a flatbed optical transmission scanner (ESI S4†). We converted the optical signal on a pixel-by-pixel basis into film thickness and searched for localized regions of negligible thickness. In this way, we could not find any locally thin regions (pinholes) of size larger than the resolution of the scanner (~10 μm), even when probing a relatively large area ~1 cm^2 for film thicknesses as low as 66 nm. This supports our assessment that continuous and uniform nanosheet networks were obtained by spray coating.

Cross-sectional images of the fabricated devices using I-SWNT and S-SWNT were obtained using focused ion beam milling followed by SEM, as shown in Fig. 2E and F respectively. It can be seen that the WS_2 nanosheet networks are sandwiched between the solution-processed top electrodes and ITO bottom electrodes. The highly porous structure of WS_2 networks is observed and the porosity is estimated to be around 50% (ESI, S5†), in line with previous results.[8] The thicknesses of WS_2 networks used to produce these two images are about 6.4 μm and 2.6 μm, respectively, values which are consistent with those found by profilometry (6 μm and 2.5 μm). In these cross sections, the top electrode, made from either I-SWNTs/AgNWs or S-SWNTs, sits on top of the WS_2 network. No visible nanowire/nanotubes are diffusing into the network, which is true even for thin networks (~600 nm thick WS_2, Fig. S4A and B†). This confirms our expectation that 1D nanomaterials could form a network on top of nanosheet network without solvent-driven inter-layer mixing. This is an important result as it shows that a clean interface can be formed during sequential spray deposition. We note that the interface quality is largely affected by the roughness of the underlying layer. The smooth ITO surface forms a sharp interface with WS_2. However, while the SWNT top electrodes form a locally clean interface with the WS_2, over longer horizontal length scales, the interface does display some peak-and-valley character due to spatial variations in the thickness of the WS_2 network (*i.e.* roughness). Depending on the mean thickness of the WS_2 network, the thickness difference between the peak and valley could be hundreds of nanometers.

The top-view SEM image of a top electrode fabricated from an I-SWNTs network coated with an AgNW network (both on WS_2) is shown in Fig. 2G. The I-SWNTs/AgNWs are uniformly distributed on the surface of the WS_2 film and form an open, porous structure. WS_2 nanosheets are still visible through this double-layered electrode. In contrast, S-SWNTs are densely packed on the top of WS_2 films (Fig. 2H).

The thickness and morphology of these top electrodes were also characterized by profilometry. To do this, I-SWNTs, S-SWNTs and I-SWNTs/AgNWs films were sprayed directly onto pre-cleaned glass slides. We find the mean film thickness $\langle t\rangle$ of the I-SWNTs film is around 80 nm but it shows a high average roughness $\langle R_a\rangle$ of about 60 nm. Such large $\langle R_a\rangle$ may indicate that aggregates formed during spraying due to instability of SWNTs in IPA. The S-SWNTs film is around 650 nm thick and had a $\langle R_a\rangle$ of about 50 nm, consistent with good network uniformity. The $\langle t\rangle$ of I-SWNTs/AgNWs film is 260 nm with a $\langle R_a\rangle$ of 60 nm. It should be possible to further optimize the roughness in the future. However, for now it is good enough to be used as the top electrode.

In-plane electrical characterization of electrodes

We start by measuring the in-plane electrical properties of the electrodes. The I-SWNTs, I-SWNTs/AgNWs and S-SWNTs were separately sprayed on glass substrates. Their electrical resistances were measured by a two-probe measurement using silver paste as contacts. The in-plane conductivities of I-SWNTs and S-SWNTs films were found to be relatively low: 1.8×10^3 and 6.8×10^3 S m^{-1}, respectively. This means that the in-plane resistance of the top electrodes is not negligible compared to the out-of-plane resistance of WS_2. This is significant as, in these devices, current flows first through the top electrode in the in-plane direction before flowing through the WS_2 in the out-of-plane direction. Then, if the in-plane SWNT resistance, is non-trivial compared to the out-of-plane WS_2 resistance, the voltage drop across the device will not be the same as the applied voltage, leading to an incorrect calculation of WS_2 network properties. This effect is shown schematically in Fig. S5† and an example of the calculation is shown in ESI S6.† Thus, two different strategies were used to remove the influence of the electrode. In the first case, AgNWs was sprayed on top of I-SWNTs to reduce the in-plane resistance. This led to a conductivity of the I-SWNTs/AgNWs film of ~5×10^5 S m^{-1} (which may still be underestimated due to the effect of contact resistance coming from the two-probe measurement). It was also found that AgNWs did not alter the shape of current–voltage (*I–V*) characteristic curves of devices, indicating that they do not change the nature of charge injection (see below). In the second case, for S-SWNTs based devices, AgNWs were not used to increase the electrode conductivity, as we found AgNWs to be in contact with WS_2 at the edge of electrodes due to spray coating through the shadow mask, which will eliminate the diode behavior (Fig. S7E†). Instead, we used the conductivity determined from the SWNTs film on the glass coupled with the electrode dimensions, to estimate the electrode resistance and remove its effect from the *I–V* curves. The detailed method is in ESI S6.† We used the second strategy for S-SWNTs electrode-based devices.

Electrical characterization of devices

The electrical response of thin semiconductor films can be limited by either the properties of the semiconductor itself or the properties of the metal–semiconductor interface.[20] In the former case, we refer to the conduction as being bulk-limited while in the latter case, it is electrode-limited. Bulk-limited devices are those where the resistance of the semiconductor itself is much greater than that associated with the interface (*i.e.* the contact resistance) while electrode-limited devices are those where the resistance of the semiconductor can be neglected. In some cases, the bulk resistance can be similar to that of the interface. Then the device can display bulk- or electrode-limited regimes depending on the applied voltage.

In-plane electrical characterization of WS_2 networks

We first perform basic electrical characterization of the WS_2 networks. We do this by measuring the in-plane conductivity of these networks as this is the most common reported measurement method.[12] In-plane measurements on networks are usually performed with a long channel length which generally yields bulk-limited conduction. However, ideally, Ohmic contacts should also be used to minimize contact resistance. In a p-type[8] material such as WS_2, Ohmic contact can be realized when the work function (WF) of the electrode material lies between the Fermi energy (E_f) and the valence band edge of the semiconductor. In this case, when the metal contacts WS_2, its bands only bend slightly in a way that leads to minimal built-in voltage, allowing carriers to flow freely across the contact. The Fermi energy of bulk-like WS_2 nanosheets produced by LPE has been reported to be −4.8 eV (ref. 37) (for completeness the conduction band minimum (CBM) is reported to be −4.2 eV,[37] while taking the bandgap of ∼1.2 eV, the valence band maximum (VBM) is then around −5.4 eV). However, the doping state and hence Fermi energy of TMDs will depend on processing conditions (*e.g. via* residual solvent *etc.*), meaning we might expect E_f vary to somewhat from this value. The widely cited WF for ITO is −4.7 eV.[38] It is conceivable that, for our WS_2, E_f is deeper than −4.7 eV leading to Ohmic contact at the ITO/WS_2 interface.

Thus, to measure WS_2 conductivity in the horizontal, in-plane (IP) direction, we fabricated ITO/WS_2/ITO devices as follows. A pre-patterned gap was etched onto ITO-coated glass, leading to two separate ITO electrodes. The gap between ITO pads led to a channel length L of ∼1 mm and a channel width W of ∼10 mm. A WS_2/IPA dispersion was sprayed onto ITO-coated glass leading to networks covering both gap and electrodes. Multiple networks were made with thicknesses varying from 465 nm to 1568 nm. One typical device image is shown in Fig. S8.† The semi-log I–V curves of these devices measured from −5 to 5 V are shown in Fig. 3A, with the equivalent linear plots shown in its inset. The curves are linear and symmetric and exhibit thickness-dependent properties with current falling with increasing film thickness, exactly as expected for bulk limited devices. These curves yielded very similar conductivities for all thicknesses with a mean of 2×10^{-3} S m^{-1}. This is considerably higher than previous reports on liquid-exfoliated[39] WS_2, but similar to that reported for dry-deposited WS_2 networks.[40]

Out of plane characterization of bulk-limited devices

While in-plane conductivity measurements on nanosheet networks are widely reported,[12] out-of-plane measurements are much less common because of problems with shorting in thin sandwich-structure devices.[12] Here, we first focus on sandwich-structure devices with ITO as bottom electrode and I-SWNTs as the top electrode. For each substrate, four independent devices were fabricated. Here we measure the vertical current flowing through the WS_2 in the out-of-plane (OoP) direction. The I–V characteristics of the devices were measured in the range of −3 to 3 V. The current density J was obtained by dividing I by the measured device area A. Fig. 3B shows one typical J–V curve of ITO/∼1.2 μm WS_2/I-SWNTs/AgNWs device. The curve is symmetrical and shows a linear behavior at low biases which is consistent with Ohmic conduction as described by $J = \sigma E$, where σ is the electrical conductivity. The electric field E is calculated by dividing the voltage drop across WS_2 by its mean thickness, t.

These results above imply that this device to be Ohmic. We have already argued that the ITO/WS_2 interface can be Ohmic depending on the doping state of the WS_2. However, we must also consider the nature of the WS_2/I-SWNTs interface. The WF of SWNTs film after acid-treatment is reported to be −5 eV,[33] slightly greater than the pristine value of −4.8 eV.[41] Thus, so long as the E_f of WS_2 is not deeper than −5 eV, we expect Ohmic contact at this top interface. The energy band diagram of each material is presented in the inset of Fig. 3B.

It should be noted that because the coverage of I-SWNTs on top of the WS_2 film is not 100% as seen from SEM, it is possible that AgNWs may be in contact with WS_2. We performed a study in ESI S7,† comparing the electrical properties of the device with and without AgNWs. Indeed, identical J–V behaviors were observed for devices without and with AgNWs

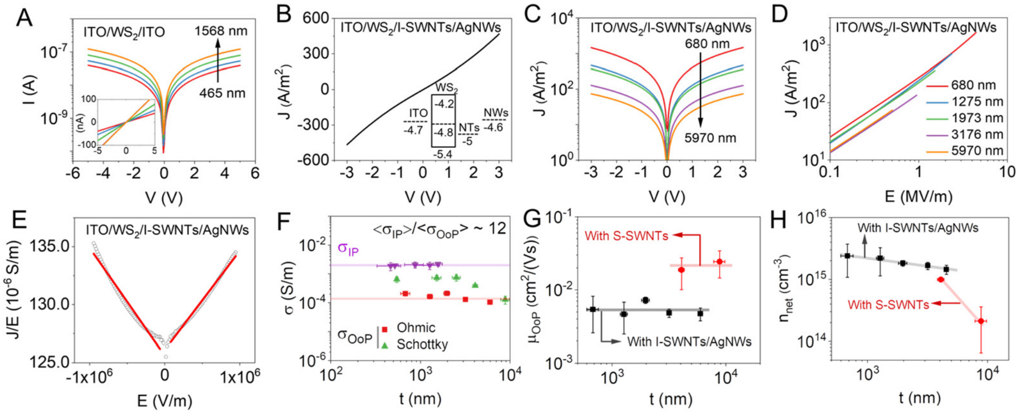

Fig. 3 Electrical characterizations and properties of Ohmic devices. (A) Semi-log I–V curves of lateral ITO/WS_2/ITO devices with various WS_2 thickness and inset is the linear I–V curves. (B) A representative J–V curve of an ITO/1.2 μm WS_2/I-SWNTs/AgNWs device. (C) Semi-log J–V curves and (D) log–log J–E curves of ITO/WS_2/I-SWNTs/AgNWs devices with various WS_2 thicknesses. (E) A typical J/E–E curve of an ITO/WS_2/I-SWNTs/AgNWs device. (F) The in-plane and out-of-plane conductivity of WS_2 networks with Ohmic contacts plotted *versus* network thickness. In addition, the OoP conductivity estimated from the electrode limited devices is also shown. (G) and (H) show the WS_2 film thickness dependence of the OoP mobility μ_{OoP} and carrier density n_{net} extracted either from I-SWNTs/AgNWs based or from S-SWNTs based devices, respectively. In F, G and H, the error bars represent averages over four independent devices per thickness.

(Fig. S7†). However, using I-SWNTs/AgNWs double-layered electrodes gives the advantage that the resistance of this type of electrode is negligible compared to that of the WS_2, significantly simplifying data analysis.

The discussion above implies the devices using I-SWNTs as the top electrode have Ohmic contacts on both top and bottom and so are bulk-limited. We can confirm this by examining *J*–*V* curves for devices with different WS_2 thicknesses. Purely electrode-limited devices should show no dependence on semiconductor thickness. Several devices with various WS_2 film thicknesses, *t*, using I-SWNTs/AgNWs as top electrodes were fabricated, and their typical *J*–*V* curves are shown in Fig. 3C (all curves are shown in Fig. S9†). We find all *J*–*V* curves to be symmetric, and exhibit thickness-dependent properties with *J* falling with increasing film thickness, exactly as expected for bulk limited devices. As the voltage drop on the I-SWNT/AgNW electrodes is negligible, *E* can be estimated by directly dividing the bias voltage *V* by *t*. The *J*–*E* curves are plotted in Fig. 3D and almost perfectly overlap with each other. This is what we would expect for a bulk-limited devices with the current flow controlled by WS_2 conductivity and electrode dimensions.

While we might expect Ohmic contacts at both top and bottom electrodes to result in purely linear *J*–*V* curves, slight curvature appears at higher biases in the *J*–*V* curve (Fig. 3B and D). This nonlinearity of *J* does not mean we have electrode-limited conduction as might be found in a Schottky diode. There are a number of bulk conduction mechanisms that can lead to such non-linearities.[20] One common mechanism that becomes visible at higher biases is space charge limited conduction (SCLC) which leads to a contribution to the current density as described by the Mott–Gurney law:[42]

$$J = \frac{9}{8}\varepsilon_0\varepsilon_r\mu\frac{E^2}{L} \quad (1)$$

where ε_0 and ε_r are the vacuum permittivity and the relative permittivity of WS_2, respectively while μ is the mobility of WS_2. This equation is usually adopted to describe symmetric, Ohmic-contacted, single carrier devices.[43] In our case, ITO and I-SWNTs both have deep work functions and, as we have argued above, display reasonable Ohmic behaviors. Considering LPE WS_2 is a p-type material,[8] we expect the hole current to dominate in our devices. Thus, we expect these conditions to apply reasonably well here. We note that Yu *et al.*[44] reported electron-only SCLC in stacked ITO/TiO_2/MoS_2/Al devices although the presence of the TiO_2 hole-blocking layer does mean some deviation from the conditions listed above.

Eqn (1) allows OoP electrical properties of MoS_2 to be extracted in these device structures. Usually, SCLC analysis is done by identifying a high-voltage regime where the current scales as voltage squared and fitting using eqn (1). However, the curvature in Fig. 3D is very weak indicating that SCLC is not dominant in the voltage range under study.

To analyze the current–voltage data for the ITO/WS_2/I-SWNTs/AgNWs devices, we assume that Ohmic and space charge currents flow in parallel. Although this is not perfectly accurate, it is known to be a very good approximation.[45] Then, the total current density is given by an addition of both types of currents:

$$J = \sigma E + \frac{9}{8}\varepsilon_0\varepsilon_r\mu\frac{E^2}{L}. \quad (2)$$

This equation can be re-arranged to give eqn (3).

$$J/E = \sigma_{OoP} + \frac{9}{8}\varepsilon_0\varepsilon_r\mu_{OoP}\frac{E}{L} \quad (3)$$

where we add the subscripts OoP to signify that we use this equation to analyze out-of-plane conduction. This equation predicts a linear relationship between *J*/*E* and *E* with the intercept and the slope controlled by the OoP conductivity, σ_{OoP}, and mobility, μ_{OoP}, respectively (using the theoretical WS_2 OoP dielectric constant of 6.4 [46]). All our ITO/WS_2/I-SWNTs/AgNWs data sets give good linear curves (Fig. S10†) when plotted in this way with a fitted example shown in Fig. 3E. However, it is worth noting that assuming current addition (eqn (2)) leads to electrical properties that may be slightly under-estimated although the error is typically <10%.[45]

We extracted the OoP conductivity of these Ohmic devices and plotted it *versus* WS_2 network thickness in Fig. 3F. We find that σ_{OoP} is almost constant as expected, with a mean value of $\langle\sigma_{OoP}\rangle = 1.63 \times 10^{-4}$ S m^{-1}. In addition, the in-plane conductivity, σ_{IP}, extracted from curves in Fig. 3A is included for comparison, highlighting the thickness independence of σ_{OoP}. Using this data, we can obtain the ratio of $\langle\sigma_{IP}\rangle/\langle\sigma_{OoP}\rangle$ to be 12.3. This ratio is low compared to vacuum filtered graphene nanosheet networks which have reported values of $\langle\sigma_{IP}\rangle/\langle\sigma_{OoP}\rangle$ between 20 and 1000, depending on porosity.[47] We note that Barwich *et al.*[47] showed that the conductivity anisotropy also depends on the dimensions of the nanosheets. The maximum conductivity anisotropy (assuming perfect alignment) in a network is related to the mean length $\langle L_{NS}\rangle$ and mean thickness $\langle t_{NS}\rangle$ of the nanosheets *via*:

$$\langle\sigma_{IP}\rangle/\langle\sigma_{OoP}\rangle = (\langle L_{NS}\rangle/\langle t_{NS}\rangle)^2. \quad (4)$$

In our case, the upper limit of the conductivity ratio can be found to be ~100. We expect the reduced conductivity anisotropy observed here is due to the open nature of the sprayed network (Fig. 2E and F) and the relatively low nanosheet alignment.

The obtained values of μ_{OoP} are shown in Fig. 3F and are constant with thickness with a mean value of $\langle\mu_{OoP}\rangle = 5.3 \times 10^{-3}$ cm^2 V^{-1} s^{-1} (Fig. 3G). Because the carrier density is the same regardless of conduction direction, we expect $\sigma_{OoP}/\sigma_{IP} = \mu_{OoP}/\mu_{IP}$. Then, taking $\langle\sigma_{IP}\rangle/\langle\sigma_{OoP}\rangle = 12.3$, we find $\langle\mu_{IP}\rangle = 6.5 \times 10^{-2}$ cm^2 V^{-1} s^{-1}. This is consistent with the IP values of ~0.01 cm^2 V^{-1} s^{-1}, ~0.1 cm^2 V^{-1} s^{-1} and ~0.2 cm^2 V^{-1} s^{-1} for liquid exfoliated WS_2 obtained by Higgins *et al.*,[48] O'Suilleabhain *et al.*[49] and Kelly *et al.*[8] respectively.

The network carrier density, n_{net}, can be calculated by using $n_{net} = \sigma_{OoP}/q\mu_{OoP}$ and is plotted in Fig. 3H as a function of WS_2 thickness. This curve shows a slight decrease with increasing thickness possibly due to substrate doping effect associated with charge transfer from one of the electrodes to the WS_2. The mean carrier density is 1.9×10^{15} cm^{-3}, which is close to the previously reported value of 5.8×10^{15} cm^{-3}.[50] The carrier density is lower than the individual multi-layered flake value ($\sim 10^{17}$ cm^{-3}),[51] which could be due to the residual doping effect during solution processing.[12]

Out-of-plane electrode limited devices

Having shown that the ITO/WS_2/I-SWNTs devices are Ohmic, we move on to a slightly different device, where we replace isopropanol-dispersed SWNTs with surfactant-suspended SWNTs (S-SWNTs): ITO/WS_2/S-SWNTs. For these devices, we didn't spray AgNWs on top as we found that rectifying behaviors to be lost, probably due to undesired AgNWs/WS_2 contacts at the electrode edge caused during spray coating (Fig. S7E†). Thus, all *I–V* curves with S-SWNTs as the top electrode are corrected by subtracting the voltage drop on the S-SWNTs top electrode as indicated above (see section S6, original curves in Fig. S11 and corrected ones in Fig. S12†). In the ESI,† we have described in detail the assumptions required to perform this correction. We also justify these assumptions and show that, even though the S-SWNTs electrode has relatively low conductivity, the top electrode has low enough resistance to result in a uniform current flow through the entire active area of the WS_2 film.

We prepared a set of ITO/WS_2/S-SWNTs devices with different WS_2 thickness and measured the *I–V* curve from −3 to 3 V and then from 3 to −3 V, denoting these the first and the second sweeps, respectively. A typical *J–V* curve for the device of ITO/1.5 μm WS_2/S-SWNTs is shown in Fig. 4A. This curve is clearly very different from these shown in Fig. 3A and B for Ohmic devices as it shows an obvious rectifying behavior with a noticeable hysteresis. The hysteresis is most obvious for the 1.5 μm and 2.5 μm WS_2 thick devices, and it may be caused by interfacial trap states in our devices at WS_2/S-SWNTs interfaces.[52] As we later found that the extracted parameters from the second sweep gave better agreement with those from Ohmic devices, we mainly focus on the *J–V* curves from the second sweep for the following analysis. The analysis on the hysteresis is presented in ESI S16.†

From the results of the ITO/WS_2/I-SWNTs/AgNWs devices, we know that Ohmic contact is realized at ITO/WS_2 interface. Thus, the rectifying behavior is likely due to a potential barrier at the WS_2/S-SWNTs interface yielding Schottky diodes rather than Ohmic devices. To create such potential barrier, the Fermi energy of either the WS_2 or the S-SWNTs has to be different from the values described above. However, SDBS is not an effective dopant for SWNTs and there is no evidence from the UV-Vis-NIR absorption and Raman spectra of the S-SWNT that their electronic structure is altered by SDBS. Alternatively, Biccai *et al.*[53] found that poly(ethylene oxide) could dope MoS_2 nanosheets, leading to at least one order of magnitude increase in network conductivity. Thus, it is more likely that SDBS dopes the interfacial WS_2 in some way, shifting its E_f, leading to the formation of a potential barrier at the WS_2/S-SWNTs interface. Given that the cathode is on the S-SWNTs side, the anode is on the ITO side, and the rectification appears on the positive applied voltage, this implies that positive applied voltage should lower the potential barrier. Thus, the E_f of doped WS_2 should be deeper than its pristine value. The possible energy band diagram is illustrated in Fig. 4A inset.

Second sweep *J–V* curves for ITO/WS_2/S-SWNTs devices with different WS_2 thicknesses are shown in Fig. 4B. The full set of *J–V* curves are shown in Fig. S12.† Interestingly, as WS_2 thickness increases, the *J–V* curves appear to exhibit a range of behaviors. For the thinnest films, *J* increases rapidly with *V* for both negative and positive polarities. However, as the thickness is increased, the curves become more diode-like with

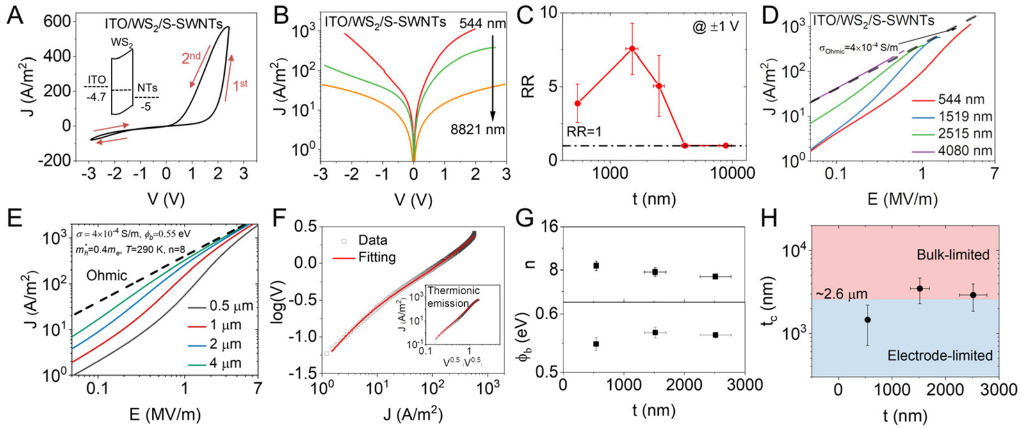

Fig. 4 Electrical characterizations and properties of Schottky devices. (A) A typical *J–V* curve of ITO/1.5 μm WS_2/S-SWNTs device after removing voltage drop on the S-SWNTs electrode. The inset in (A) is the band diagram of ITO, WS_2, and S-SWNTs. (B) Semi-log *J–V* curves of ITO/WS_2/S-SWNTs devices with various WS_2 thicknesses. (C) Rectification ratio of ITO/WS_2/S-SWNTs devices at ± 1 V for the second sweep. (D) *J–E* curves of ITO/WS_2/S-SWNTs devices with various WS_2 thicknesses. (E) Simulated *J–E* curves with various thicknesses. (F) A typical log(*V*)–*J* curve of a Schottky device and its fitting curve. The inset in (F) is one typical J–$V^{0.5}$ curve. (G) is extracted thickness-dependent ideality factor *n* (top) and potential barrier ϕ_b (bottom), respectively. (H) is the plot of the transition film thickness t_c *versus* WS_2 film thickness. In C, G and H, the error bars represent averages over four independent devices per thickness.

much reduced currents at negative voltage. However, for the thickest films, the curves become much more symmetric, resembling those shown in Fig. 3C. We interpret this behavior as a transition from back-to-back (B2B) Schottky-type behavior[54] to normal (single) Schottky diode behavior, and finally to Ohmic behavior as WS_2 network thickness is increased.

The device with the thinnest WS_2 layer (ITO/544 nm WS_2/S-SWNTs) shows roughly exponential increases of J for both polarities above transition voltages of about 0.5 and −1 V (Fig. S12A†). This strong super-linear behavior is much more pronounced than the slight curvature seen in the Ohmic devices in Fig. S9A† (for a comparable WS_2 thickness). We believe this behavior implies Schottky barriers at both electrodes which is due to shifts in the WS_2 Fermi energy throughout the thin film. The nanosheet networks are highly porous (Fig. 2E and F) so residual H_2O/SDBS could easily diffuse into the network from the top electrode during spraying. Thus, for this very thin film (544 nm), we propose that SDBS has diffused throughout the entire network, even reaching the ITO/WS_2 interface. This leads to enough doping to shift the Fermi level everywhere, resulting in band bending and potential barriers at both top and bottom electrodes.

For the medium WS_2 thicknesses (1.5–2.5 μm), clear rectification is observed, consistent with single Schottky diode behavior. We propose that SDBS has only diffused slightly into the WS_2 network, leading to doping only in the vicinity of the top electrode, leaving the ITO/WS_2 interface un-changed. For the thicker films (>4 μm), symmetric, Ohmic-like behavior is observed. This is possible when the high WS_2 thickness leads to the WS_2 network acting as a large series resistance. Once this series resistance becomes larger than the Schottky contact resistance, the thick film devices become bulk limited.

To visualize this thickness-induced transition, we plot the rectification ratios (RR) of these devices, measured at ± 1 V, *versus* film thickness for the second sweep in Fig. 4C (see also Fig. S13†). RR is defined as the ratio of J at the same applied voltage with opposite polarity and manifests the ability of the diode to rectify current. The RRs for the three thinnest devices are ∼3–10, falling to 1 for the two thickest devices, behavior which is consistent with the hypothesis given above. The RRs from the thinner devices are lower than previously reported Schottky diodes based on LPE nanosheet with a vertical MSM structure,[27] which were around 40–110 at ≤± 2 V. It may be caused by several factors, such as a large leakage current,[55] a high series resistance[56] or a poor interface quality.[57] The RR reaching 1 shows that the transition to bulk-limited behavior is complete by a WS_2 thickness of 4 μm.

The forward bias (positive polarity) parts of the current–voltage characteristics for different WS_2 thicknesses are plotted as J *versus* electric field, E (where $E = V/t$), on a log–log basis in Fig. 4D. For Schottky diodes with thin WS_2 films (*e.g.* 544 nm), at lower electrical fields holes have insufficient energy to overcome the potential barrier leading to low currents which scale roughly linearly with E. Such devices are thus electrode-limited at low voltage. As the voltage is increased, the potential barrier is lowered resulting in an exponential increase of J. However, at relatively higher electrical field, when the potential barrier is greatly reduced, the voltage drop across the interface becomes less than the series resistance of the WS_2, and the device becomes bulk-limited. At this point the device should carry the same current as the equivalent Ohmic device. This is exactly what is observed in Fig. 4D with curves shifting upwards and to the left as the WS_2 thickness (and so series resistance) is increased.

The black dash line in Fig. 4E is a plot of a J–E curve representing an Ohmic device with a conductivity of 4×10^{-4} S m^{-1}, *i.e.* that of the Ohmic devices shown in Fig. 3. The thicker ITO/∼4 μm WS_2/S-SWNTs device, which we expect to be bulk limited, matches this curve very well. The thinner devices, appear to approach this Ohmic line at high applied voltage, in line with their expected transition to being bulk limited. Indeed, the current densities for devices with rectifying behavior are all below this line, confirming they are all electrode-limited at lower E.

When MSM systems are modelled as Schottky diodes, it is usually assumed that there is a Schottky barrier at one electrode, but Ohmic contact at the other. In addition, it is assumed that the resistance associated with the semiconductor can be neglected. Then, the current density J is given by eqn (5).[58]

$$J = J_s[\exp(qV_c/nkT) - 1] \tag{5}$$

where J_s is the saturation current density, V_c is the voltage drop across the Schottky barrier (equal to the voltage drop across the entire device within these approximations), n is the ideality factor, q is the elementary charge, k is the Boltzmann constant and T is temperature. For 3D systems, J_s is defined as

$$J_s = A^*T^2 \exp(-q\phi_b/kT) \tag{6}$$

where A^* is Richardson constant, h is Planck constant, ϕ_b is the barrier height (defined as the difference between the work function of the metal and the valence band maximum of the semiconductor).

In order to model our J–V curves, we must consider the contribution of the series resistance of WS_2. This is included by writing V_c as the applied voltage, V, minus the voltage drop across the WS_2 layer:[58]

$$J = J_s[\exp(q(V - JR_sA/nkT) - 1] \tag{7}$$

where R_s is the series resistance of WS_2.

We can visualize the thickness- and field dependent transition from contact-limited to bulk-limited by rewriting eqn (7) to represent electric field ($E = V/t$):

$$E = \frac{nkT}{qt}\ln\left(\frac{J\exp(q\phi_b/kT)}{A^*T^2} + 1\right) + \frac{J}{\sigma}. \tag{8}$$

We then use this equation to calculate E as a function of J using reasonable values for each parameter and for a range of thicknesses. These data sets are then plotted as J *versus* E in Fig. 4E. We find the simulated data matches well with our experimental results in Fig. 4D. This implies that the ITO/WS_2/

S-SWNTs devices are limited by both the Schottky barrier at the WS_2/S-SWNT interface and the series resistance associated with the WS_2 network with the balance of these relative contributions controlled by the relative values of contact resistance and series resistance. It is worth noting that the value of the Schottky barrier (and so the contact resistance) is controlled by the doping level of the WS_2 and so the ink formulation while the series resistance is controlled by the WS_2 network thickness. That both these parameters can be controlled allows the Schottky/Ohmic properties of these devices to be tuned.

The equation to describe J for Schottky devices assumes that the conduction is dominated by thermionic emission (TE). To verify if carriers in our Schottky devices follow TE, J is plotted against $V^{0.5}$.[59] One example is shown in Fig. 4F inset. All curves are in Fig. S14A–C.† The straight line indicates the voltage range that the obtained Schottky device follows TE. Thus, eqn (8) is used to fit log(V)–J curves in their corresponding range (details are in ESI S14†).

Based on the analysis above, we can fit the current–voltage data for our ITO/WS_2/S-SWNTs devices. The two devices with the thickest WS_2 networks are completely bulk limited and so must be fitted using eqn (3) to yield μ_{OoP} and n_{net} (after subtraction of the top electrode resistance). The thinner devices are both bulk and electrode limited (depending on voltage). There, we can use eqn (7) to fit our data which we plot as log (V) *versus* J for fitting purposes (Fig. 4F) allowing us to extract J_s, R_s and n. All fittings are presented in Fig. S14D–H.†

The obtained values of R_s are converted into conductivity σ_{OoP} and are included in Fig. 3F. The Schottky device with the thinnest WS_2 film gives σ_{OoP} about 1 order of magnitude higher than the one extracted from the Ohmic device at a comparable WS_2 thickness. σ_{OoP} decreases with t but is always higher than σ_{OoP} from Ohmic devices. The device with 8.8 μm thick WS_2 exhibits a conductivity very similar to the Ohmic ones. Such trend may be evidence of slight doping caused by SDBS. The thinnest film is affected by SDBS most while the thickest one is the least affected. Values of μ_{OoP} and n_{net} extracted from the two thickest devices were included in Fig. 4C and D, respectively. μ_{OoP} is roughly 5 times larger than the device with I-SWNTs as top electrodes, but the carrier density seems lower than the latter. The reason is still not clear and requires further investigation. However, it is worth noting that I-SWNTs/AgNWs based vertical devices and ITO/WS_2/ITO lateral devices would allow WS_2 network to interact with the ambient environment, *i.e.*, oxygen and water, which could act as p-type dopants.[60] In contrast, less interaction with ambient in S-SWNTs based devices is expected due to the visible full coverage of S-SWNTs on WS_2. There could be several times difference in electrical properties between these two types of devices.[61,62]

The ideality factor n is found to be around 7.7, and slightly decreases with t. (Fig. 4G top). Ideally, n should be in the range of 1–2 for a perfect Schottky diode although larger n values >2 have been widely reported in other solution processed Schottky diodes.[63,64] The electrical properties of the Schottky diode can be easily affected by the quality of the interface. It is known that surface roughness can greatly affect the quality of interfaces.[65] As shown in Fig. S16† sprayed WS_2 networks show surface roughness of up to 200 nm. This could lead to spatial barrier height inhomogeneity which could be one of the causes of high ideality factor. It is also likely the edge of nanosheets are oxidized in ambient conditions and forms WO_x,[66] which could also cause local barrier height variation.

The extracted J_s values are presented in Fig. S14.† Using effective hole mass $m_h^* = 0.4m_e$ (ref. 67) for WS_2 and T = 290 K, ϕ_b can be calculated from J_s using eqn (6) and is about 0.56 eV (Fig. 4G bottom). The obtained ϕ_b is slightly larger than the expected difference between the VBM of WS_2 and the WF of SWNTs of 0.4 eV.

It is worth noting that the contact resistance R_c associated with the Schottky barrier is given by $AR_c = dV_c/dJ$ in the limit of low voltage (A is the device area). Applying this to eqn (5) yields $R_c = kT/AqJ_s$.[68] Thus, in order to find the electrode-limited to bulk-limited transition film thickness t_c, we should first find $R_c = R_s$ so that devices above t_c will has a larger R_s than R_c and thus to be bulk-limited. As R_s is given by $R_s = t/(\sigma_{\text{OoP}}A)$, we can obtain $t_c = \sigma_{\text{OoP}}kT/(qJ_s)$. Using the conductivity values shown in Fig. 3F and J_s shown in Fig. S15† for the second sweep, we can find the averaged t_c is ~2.6 μm (Fig. 4H and t_c for the first sweep is given in ESI S17†). This is consistent with our results that bulk-limited behaviors are observed in devices with WS_2 thickness of 4 μm.

Conclusion

Vertical heterostructured MSM devices based on liquid exfoliated semiconducting WS_2 nanosheets and conducting SWNTs were fabricated by spray coating. Carefully adjusted spraying parameters leading to pinhole-free WS_2 nanosheet networks enable these vertical heterostructures to be realized. It was found that devices could exhibit Ohmic or Schottky behaviors depending on the composition of SWNTs dispersion. WS_2 network thickness-dependent electrical properties of devices were investigated. From Ohmic devices, we extracted values of the OoP conductivity and mobility to be in the range 1–2 × 10^{-4} S m^{-1} and 4–8 × 10^{-3} cm^2 V^{-1} s^{-1} respectively, which were roughly one order of magnitude lower than their in-plane values. The low anisotropic electrical properties along their IP and OoP directions were attributed to the porous networks formed by the random alignment of nanosheets and low aspect ratio of the nanosheet. On the other hand, the Schottky behavior may be caused by SDBS doping WS_2 nanosheet and resulted in a potential barrier at WS_2/SWNTs interface. Future work will be required for improving the morphology of nanosheet networks and exploring the mechanism of SDBS doping effect.

Author contributions

Conceptualization, methodology, investigation, and formal analysis: S. L., E.-X. D., and A. K.; investigation: L. D., C. G.,

H. K., J. M., T. C., and J. G.; conceptualization and supervision: J. C.

Conflicts of interest

There are no conflicts to declare.

Acknowledgements

We acknowledge the European Commission (Graphene Flagship Core 2 and Core 3 grant agreement No. 785219 and 881603, respectively) and the European Research Council (FUTURE-PRINT, project No. 694101). We have also received support from the Science Foundation Ireland (SFI) funded centre AMBER (SFI/12/RC/2278_P2) and availed of the facilities of the SFI-funded AML and ARL labs. T. C. acknowledges funding from a Marie Skłodowska-Curie Individual Fellowship "MOVE" (grant number 101030735, project number 211395, and award number 16883). Shixin Liu would like to express gratitude for the funding from China Scholarship Council (No. 201904910775).

References

1 K. S. Novoselov, A. K. Geim, S. V. Morozov, D. Jiang, Y. Zhang, S. V. Dubonos, I. V. Grigorieva and A. A. Firsov, *Science*, 2004, **306**, 666–669.

2 K. S. Novoselov, A. K. Geim, S. V. Morozov, D. Jiang, M. I. Katsnelson, I. V. Grigorieva, S. V. Dubonos and A. A. Firsov, *Nature*, 2005, **438**, 197–200.

3 A. G. Kelly, J. O'Reilly, C. Gabbett, B. Szydłowska, D. O'Suilleabhain, U. Khan, J. Maughan, T. Carey, S. Sheil, P. Stamenov and J. N. Coleman, *Small*, 2022, **18**, 2105996.

4 Y. Gogotsi and B. Anasori, *ACS Nano*, 2019, **13**, 8491–8494.

5 W. Armour, S. Hands and C. Strouthos, *Phys. Rev. B: Condens. Matter Mater. Phys.*, 2010, **81**, 125105.

6 Q. H. Wang, K. Kalantarzadeh, A. Kis, J. N. Coleman and M. S. Strano, *Nat. Nanotechnol.*, 2012, **7**, 699–712.

7 A. G. Kelly, D. Finn, A. Harvey, T. Hallam and J. N. Coleman, *Appl. Phys. Lett.*, 2016, **109**, 023107.

8 A. G. Kelly, T. Hallam, C. Backes, A. Harvey, A. S. Esmaeily, I. Godwin, J. Coelho, V. Nicolosi, J. Lauth, A. Kulkarni, S. Kinge, L. D. Siebbeles, G. S. Duesberg and J. N. Coleman, *Science*, 2017, **356**, 69–73.

9 S. Lu, J. A. Cardenas, R. Worsley, N. X. Williams, J. B. Andrews, C. Casiraghi and A. D. Franklin, *ACS Nano*, 2019, **13**, 11263–11272.

10 J. N. Coleman, M. Lotya, A. O'Neill, S. D. Bergin, P. J. King, U. Khan, K. Young, A. Gaucher, S. De, R. J. Smith, I. V. Shvets, S. K. Arora, G. Stanton, H. Y. Kim, K. Lee, G. T. Kim, G. S. Duesberg, T. Hallam, J. J. Boland, J. J. Wang, J. F. Donegan, J. C. Grunlan, G. Moriarty, A. Shmeliov, R. J. Nicholls, J. M. Perkins, E. M. Grieveson, K. Theuwissen, D. W. McComb, P. D. Nellist and V. Nicolosi, *Science*, 2011, **331**, 568–571.

11 Y. Hernandez, V. Nicolosi, M. Lotya, F. M. Blighe, Z. Sun, S. De, I. T. McGovern, B. Holland, M. Byrne, Y. K. Gun'Ko, J. J. Boland, P. Niraj, G. Duesberg, S. Krishnamurthy, R. Goodhue, J. Hutchison, V. Scardaci, A. C. Ferrari and J. N. Coleman, *Nat. Nanotechnol.*, 2008, **3**, 563–568.

12 A. G. Kelly, D. O'Suilleabhain, C. Gabbett and J. N. Coleman, *Nat. Rev. Mater.*, 2021, **7**, 217–234.

13 D. McManus, S. Vranic, F. Withers, V. Sanchez-Romaguera, M. Macucci, H. Yang, R. Sorrentino, K. Parvez, S. K. Son, G. Iannaccone, K. Kostarelos, G. Fiori and C. Casiraghi, *Nat. Nanotechnol.*, 2017, **12**, 343–350.

14 J. E. ten Elshof and Y. Wang, *Small Methods*, 2019, **3**, 1800318.

15 A. Capasso, F. Matteocci, L. Najafi, M. Prato, J. Buha, L. Cinà, V. Pellegrini, A. D. Carlo and F. Bonaccorso, *Adv. Energy Mater.*, 2016, **6**, 1600920.

16 A. B. Patel, H. K. Machhi, P. Chauhan, S. Narayan, V. Dixit, S. S. Soni, P. K. Jha, G. K. Solanki, K. D. Patel and V. M. Pathak, *ACS Appl. Mater. Interfaces*, 2019, **11**, 4093–4102.

17 V. Scardaci, R. Coull, P. E. Lyons, D. Rickard and J. N. Coleman, *Small*, 2011, **7**, 2621–2628.

18 D. J. Finn, M. Lotya, G. Cunningham, R. J. Smith, D. McCloskey, J. F. Donegan and J. N. Coleman, *J. Mater. Chem. C*, 2014, **2**, 925–932.

19 R. A. Shaukat, M. U. Khan, Q. M. Saqib, M. Y. Chougale, J. Kim and J. Bae, *Sens. Actuators, B*, 2021, **345**, 130371.

20 F.-C. Chiu, *Adv. Mater. Sci. Eng.*, 2014, **2014**, 1–18.

21 R. Worsley, L. Pimpolari, D. McManus, N. Ge, R. Ionescu, J. A. Wittkopf, A. Alieva, G. Basso, M. Macucci, G. Iannaccone, K. S. Novoselov, H. Holder, G. Fiori and C. Casiraghi, *ACS Nano*, 2018, **13**, 54–60.

22 Y. Nalawade, J. Pepper, A. Harvey, A. Griffin, D. Caffrey, A. G. Kelly and J. N. Coleman, *ACS Appl. Electron. Mater.*, 2020, **2**, 3233–3241.

23 A. A. Bessonov, M. N. Kirikova, D. I. Petukhov, M. Allen, T. Ryhänen and M. J. A. Bailey, *Nat. Mater.*, 2015, **14**, 199–204.

24 Y. Jo and C. Dimitrakopoulos, *IEEE Trans. Electron Devices*, 2020, **67**, 5484–5489.

25 F. Withers, H. Yang, L. Britnell, A. P. Rooney, E. Lewis, A. Felten, C. R. Woods, V. Sanchez Romaguera, T. Georgiou, A. Eckmann, Y. J. Kim, S. G. Yeates, S. J. Haigh, A. K. Geim, K. S. Novoselov and C. Casiraghi, *Nano Lett.*, 2014, **14**, 3987–3992.

26 D. McManus, S. Vranic, F. Withers, V. Sanchez-Romaguera, M. Macucci, H. Yang, R. Sorrentino, K. Parvez, S. K. Son, G. Iannaccone, K. Kostarelos, G. Fiori and C. Casiraghi, *Nat. Nanotechnol.*, 2017, **12**, 343–350.

27 M. Farbod, R. Taheri and A. Kosarian, *Appl. Mater. Today*, 2021, **24**, 101092.

28 C. Backes, D. Campi, B. M. Szydlowska, K. Synnatschke, E. Ojala, F. Rashvand, A. Harvey, A. Griffin, Z. Sofer,

N. Marzari, J. N. Coleman and D. D. O'Regan, *ACS Nano*, 2019, **13**, 7050–7061.

29 C. Backes, T. M. Higgins, A. Kelly, C. Boland, A. Harvey, D. Hanlon and J. N. Coleman, *Chem. Mater.*, 2016, **29**, 243–255.

30 C. Backes, B. M. Szydlowska, A. Harvey, S. Yuan, V. Vega-Mayoral, B. R. Davies, P. L. Zhao, D. Hanlon, E. J. Santos, M. I. Katsnelson, W. J. Blau, C. Gadermaier and J. N. Coleman, *ACS Nano*, 2016, **10**, 1589–1601.

31 W. Zhao, Z. Ghorannevis, L. Chu, M. Toh, C. Kloc, P.-H. Tan and G. Eda, *ACS Nano*, 2013, **7**, 791–797.

32 J. Kang, S. Tongay, J. Zhou, J. Li and J. Wu, *Appl. Phys. Lett.*, 2013, **102**, 012111.

33 S. Kim, J. Yim, X. Wang, D. D. C. Bradley, S. Lee and J. C. deMello, *Adv. Funct. Mater.*, 2010, **20**, 2310–2316.

34 C. Backes, R. J. Smith, N. McEvoy, N. C. Berner, D. McCloskey, H. C. Nerl, A. O'Neill, P. J. King, T. Higgins, D. Hanlon, N. Scheuschner, J. Maultzsch, L. Houben, G. S. Duesberg, J. F. Donegan, V. Nicolosi and J. N. Coleman, *Nat. Commun.*, 2014, **5**, 1–10.

35 M. L. Guaragno, R. Gottardi, M. V. Fedorchak, A. Roy, P. N. Kumta and S. R. Little, *Chem. Commun.*, 2015, **51**, 17233–17236.

36 E.-X. Ding, Q. Zhang, N. Wei, A. T. Khan and E. I. Kauppinen, *R. Soc. Open Sci.*, 2018, **5**, 180392.

37 S. K. Lee, D. Chu, J. Yoo and E. K. Kim, *Sol. Energy Mater. Sol. Cells*, 2018, **184**, 9–14.

38 B. Adilbekova, Y. Lin, E. Yengel, H. Faber, G. Harrison, Y. Firdaus, A. El-Labban, D. H. Anjum, V. Tung and T. D. Anthopoulos, *J. Mater. Chem. C*, 2020, **8**, 5259–5264.

39 G. Cunningham, D. Hanlon, N. McEvoy, G. S. Duesberg and J. N. Coleman, *Nanoscale*, 2015, **7**, 198–208.

40 W. Zhang, Q. Zhao, C. Munuera, M. Lee, E. Flores, J. E. F. Rodrigues, J. R. Ares, C. Sanchez, J. Gainza, H. S. J. van der Zant, J. A. Alonso, I. J. Ferrer, T. Wang, R. Frisenda and A. Castellanos-Gomez, *Appl. Mater. Today*, 2021, **23**, 101012.

41 P. Liu, Q. Sun, F. Zhu, K. Liu, K. Jiang, L. Liu, Q. Li and S. Fan, *Nano Lett.*, 2008, **8**, 647–651.

42 J. A. Rohr, D. Moia, S. A. Haque, T. Kirchartz and J. Nelson, *J. Phys.: Condens. Matter*, 2018, **30**, 105901.

43 V. M. Le Corre, E. A. Duijnstee, O. El Tambouli, J. M. Ball, H. J. Snaith, J. Lim and L. J. A. Koster, *ACS Energy Lett.*, 2021, **6**, 1087–1094.

44 X. Yu, M. S. Prévot and K. Sivula, *Chem. Mater.*, 2014, **26**, 5892–5899.

45 W. P. Dumke, *Solid-State Electron.*, 1982, **25**, 101–103.

46 A. Laturia, M. L. Van de Put and W. G. Vandenberghe, *npj 2D Mater. Appl.*, 2018, **2**, 1–7.

47 S. Barwich, J. Medeiros de Araújo, A. Rafferty, C. Gomes da Rocha, M. S. Ferreira and J. N. Coleman, *Carbon*, 2021, **171**, 306–319.

48 T. M. Higgins, S. Finn, M. Matthiesen, S. Grieger, K. Synnatschke, M. Brohmann, M. Rother, C. Backes and J. Zaumseil, *Adv. Funct. Mater.*, 2019, **29**, 1804387.

49 D. O'Suilleabhain, V. Vega-Mayoral, A. G. Kelly, A. Harvey and J. N. Coleman, *ACS Appl. Mater. Interfaces*, 2019, **11**, 8545–8555.

50 J. H. Kim, S. Yu, S. W. Lee, S.-Y. Lee, K. S. Kim, Y. A. Kim and C.-M. Yang, *Crystals*, 2020, **10**, 140.

51 A. Matthäus, A. Ennaoui, S. Fiechter, S. Tiefenbacher, T. Kiesewetter, K. Diesner, I. Sieber, W. Jaegermann, T. Tsirlina and R. Tenne, *J. Electrochem. Soc.*, 1997, **144**, 1013–1019.

52 V. Ulianova, Y. Didenko, S. Bolat, G. T. Sevilla, D. Tatarchuk, I. Shorubalko, E. Gilshtein and Y. E. Romanyuk, *AIP Adv.*, 2020, **10**, 075104.

53 S. Biccai, C. S. Boland, D. P. O'Driscoll, A. Harvey, C. Gabbett, D. R. O'Suilleabhain, A. J. Griffin, Z. Li, R. J. Young and J. N. Coleman, *ACS Nano*, 2019, **13**, 6845–6855.

54 A. Grillo and A. Di Bartolomeo, *Adv. Electron. Mater.*, 2020, **7**, 2000979.

55 S. Dongaonkar, J. D. Servaites, G. M. Ford, S. Loser, J. Moore, R. M. Gelfand, H. Mohseni, H. W. Hillhouse, R. Agrawal, M. A. Ratner, T. J. Marks, M. S. Lundstrom and M. A. Alam, *J. Appl. Phys.*, 2010, **108**, 124509.

56 C. D. Lien, F. C. T. So and M. A. Nicolet, *IEEE Trans. Electron Devices*, 1984, **31**, 1502–1503.

57 M. C. Newton, S. Firth and P. A. Warburton, *Appl. Phys. Lett.*, 2006, **89**, 072104.

58 S. K. Cheung and N. W. Cheung, *Appl. Phys. Lett.*, 1986, **49**, 85–87.

59 J. C. Tinoco, M. Estrada, B. Iñiguez and A. Cerdeira, *Microelectron. Reliab.*, 2008, **48**, 370–381.

60 H. Schmidt, F. Giustiniano and G. Eda, *Chem. Soc. Rev.*, 2015, **44**, 7715–7736.

61 Q. Liang, J. Gou, Arramel, Q. Zhang, W. Zhang and A. T. S. Wee, *Nano Res.*, 2020, **13**, 3439–3444.

62 P. Han, E. R. Adler, Y. Liu, L. St Marie, A. El Fatimy, S. Melis, E. Van Keuren and P. Barbara, *Nanotechnology*, 2019, **30**, 284004.

63 A. G. Martinez-Lopez, W. Y. Padron-Hernandez, D. Pourjafari, G. Oskam, G. Rodriguez-Gattorno, M. Estrada and J. C. Tinoco, *IEEE Electron Device Lett.*, 2018, **39**, 1940–1943.

64 K.-Y. Chan, Z.-N. Ng, B. W.-C. Au and D. Knipp, *Opt. Mater.*, 2018, **75**, 595–600.

65 D. Drdlik, Z. Chlup, H. Hadraba and K. Drdlikova, *J. Aust. Ceram. Soc.*, 2019, **56**, 721–727.

66 L. Karger, K. Synnatschke, S. Settele, Y. J. Hofstetter, T. Nowack, J. Zaumseil, Y. Vaynzof and C. Backes, *Adv. Mater.*, 2021, **33**, 2102883.

67 I. Tanabe, M. Gomez, W. C. Coley, D. Le, E. M. Echeverria, G. Stecklein, V. Kandyba, S. K. Balijepalli, V. Klee, A. E. Nguyen, E. Preciado, I. H. Lu, S. Bobek, D. Barroso, D. Martinez-Ta, A. Barinov, T. S. Rahman, P. A. Dowben, P. A. Crowell and L. Bartels, *Appl. Phys. Lett.*, 2016, **108**, 252103.

68 S. M. Sze, *Semiconductor Devices*, John Wiley and Sons, 1985.